Applied Radiation and Isotopes 129 (2017) 19–27

Contents lists available at ScienceDirect

Applied Radiation and Isotopes

journal homepage: www.elsevier.com/locate/apradiso

Optimization of the sensitivity/doses relationship for a bench-top EDXRF system used for in vivo quantification of gold nanoparticles

M. Santibáñez[a,b,*], R. Saavedra[a], M. Vásquez[a], F. Malano[c,d], P. Pérez[c,d], M. Valente[a,b,c,d], R.G. Figueroa[a,b]

[a] Departamento de Ciencias Físicas, Universidad de la Frontera, Avda. Francisco Salazar, 01145 Temuco, Chile
[b] Centro de Física e Ingeniería en Medicina (CFIM), Facultad de Ingeniería y Ciencias, Universidad de La Frontera, Temuco, Chile
[c] Instituto de Física E. Gaviola, CONICET & FaMAF – Universidad Nacional de Córdoba, Ciudad Universitaria, 5000 Córdoba, Argentina
[d] Laboratorio de Investigación e Instrumentación en Física Aplicada a la Medicina e Imágenes por Rayos X – LIIFAMIRX, FaMAF – Universidad Nacional de Córdoba, Córdoba, Argentina

HIGHLIGHTS

- High sensitivity and minimum surface doses for in vivo GNPs quantification.
- Determination of agents for tumor marker and targeting radiotherapy.
- Bench top EDXRF system for monitoring nanoparticles in biomedical application.

ARTICLE INFO

Keywords:
Gold nanoparticles
Tumor biomarkers
Targeting radiotherapy
In vivo EDXRF
Bench top L-XRF

ABSTRACT

The present work is devoted to optimizing the sensitivity-doses relationship of a bench-top EDXRF system, with the aim of achieving a detection limit of 0.010 mg/ml of gold nanoparticles in tumor tissue (clinical values expected), for doses below 10 mGy (value fixed for in vivo application). Tumor phantoms of 0.3 cm^3 made of a suspension of gold nanoparticles (15 nm AurovistTM, Nanoprobes Inc.) were studied at depths of 0–4 mm in a tissue equivalent cylindrical phantom. The optimization process was implemented configuring several tube voltages and aluminum filters, to obtain non-symmetrical narrow spectra with fixed FWHM of 5 keV and centered among the 11.2–20.3 keV. The used statistical figure of merit was the obtained sensitivity (with each spectrum at each depth) weighted by the delivered surface doses. The detection limit of the system was determined measuring several gold nanoparticles concentrations ranging from 0.0010 to 5.0 mg/ml and a blank sample into tumor phantoms, considering a statistical fluctuation within 95% of confidence. The results show the possibility of obtaining a detection limit for gold nanoparticles concentrations around 0.010 mg/ml for surface tumor phantoms requiring doses around 2 mGy.

1. Introduction

Recently, different nanoparticles have been functionalized to act as tumor markers as well as to be simultaneously applied on highly localized treatments. Gold nanoparticles (GNPs), which have been the object of most of the conducted studies, are enhancers of local absorbed dose for orthovoltage radiotherapy (Hainfeld et al., 2013, 2004; Ngwa et al., 2014) as well as a contrast agent with better attenuation than the traditionally used compounds (Hainfeld et al., 2013, 2006). The advances achieved in this field have proposed the future use of the nanoparticles for the detection of small clusters of infiltrating cancer, providing information about tumor characteristics to map the disease state, and generating images to produce personalized cancer therapy regimes (Ricketts et al., 2012). One of the common challenges faced when using these new agents is the need to develop methodologies for detection: in vivo, quick, efficient, with greater sensitivity and lower doses in those cases involving, organisms. Given the above, effectiveness assessment of nanoparticles applications requires precise knowledge of the concentration and distribution in the volumes to be studied.

Several authors have proposed a number of systems capable to identify and quantify GNPs showing different detection limits. The most studied devices were the conventional computed tomography (CT) and the micro-CT systems with predictive sensitivities of up to 0.50 mg/ml for in vivo studies using X-ray equipment at operation energies up to

* Corresponding author at: Departamento de Ciencias Físicas, Universidad de la Frontera, Avda. Francisco Salazar, 01145 Temuco, Chile.
E-mail address: mauricio.santibanez@ufrontera.cl (M. Santibáñez).

http://dx.doi.org/10.1016/j.apradiso.2017.08.006
Received 16 December 2016; Received in revised form 2 August 2017; Accepted 3 August 2017
Available online 04 August 2017
0969-8043/

140 kVp (Hainfeld et al., 2011, 2010; Popovtzer et al., 2008). However, CT and micro-CT techniques do not allow simultaneous distinction between the different types of nanoparticles embedded in the tumor. The X-ray fluorescence (XRF) was quickly included in the study of nanoparticles, given that the magnitude of the XRF signal is proportional to the concentration of the element, and the energy of the fluorescence indicates elemental composition, offering advantages compared to the devices based only on the attenuation of the incident beam. XRF studies enabled multi-parametric imaging and the possibility of correlating these parameters to two or more specific characteristics of tumor tissues under study (Ricketts et al., 2012, 2013). Highly monochromatic X-rays (produced by synchrotron facilities) allowed higher sensitivity due to excitation with spectra just above and below the absorption edge (thus, maximizing the production of X-rays and allowing optimal subtraction of the background). These studied have reported extremely low detection limits for GNPs (< 0.0050 mg/ml) and short measuring times, thanks to the high photon flux (Ricketts et al., 2012). However, the cost and technology involved in these facilities eliminate the possibility of using such devices in future implementations in which nanoparticles are used as a routine examination.

Different experimental setups have been evaluated for quantification of GNPs by bench-top EDXRF systems, using both L and K lines for the detection, thus achieving different sensitivity ranges and depths (Manohar et al., 2013; Ren et al., 2014; Ricketts et al., 2016, 2013, 2012; Wu et al., 2013). Among measurements using L-lines, the works of Ricketts et al., (2013, 2012) report the lower detection limit (DL) for a system with an equipment of 50 kVp, obtaining an experimental DL of 0.0050 mg/ml with an acquisition time of 2000 s. Likewise, Manohar et al. (2014) performed optimization studies at various tube potentials, maximizing fluorescence photon production under the current experimental setup while maintaining the maximum beam power (50 W), obtaining a detection limit between 0.0050 and 0.050 mg/ml for an acquisition time of 600 s. However, the implemented experimental optimizations have only studied the increase in the signal for different configurations, without addressing the sensitivity/dose relationship in the application.

Monte Carlo simulation codes have also been used mainly to configure K-XRF measurement systems with the aim of increasing their sensitivity (Manohar et al., 2014; Figueroa et al., 2015; Santibañez et al., 2016a). Works performed using MCNP have initially addressed the relationship between the production of fluorescent counts versus the delivered dose and in terms of the measurement time required (Manohar et al., 2014). The energy spectrum of all X-rays sources considered had a Gaussian spread of 10 keV of FWHM and a central energy ranging from just above the gold K-edge to the maximum photon energy of the X-ray source. This configuration considered identical photon fluence in all the simulated spectra, an unrealistic condition in experimental implementation, considering that the X-ray source is operating at maximum power at all times.

In previous works reporting similar optimization procedures, detailed studies to optimize the detection limit and uncertainty by Monte Carlo simulation using the XMI-MSIM software (Figueroa et al., 2015; Santibañez et al., 2016a) were implemented. The configurations studied also considered narrow spectra of fixed width (FWHM around 9.6 keV) and a scanning in energy considering a central energy of the spectrum from 80 to 100 keV (Figueroa et al., 2015). The studied spectra considered the expected experimental spectrum (rather than theoretical analytic forms) after introducing copper filters of varying thickness and tuning the applied kVp, to produce the same FWHM, but with different central energy and different fluence, with a non-symmetrical spectral distribution (Figueroa et al., 2015; Santibañez et al., 2016a).

This paper presents the experimental configuration of a bench-top L-XRF setup capable of attaining lower in vivo concentrations of GNPs in a tumor phantom (from 0.010 mg/ml to 0.10 mg/ml), requiring the lowest surface doses to allow this range of sensitivity. The optimization process is performed improving the sensitivity-doses relationship, achieved by several non-symmetrical narrow spectra with a fixed FWHM (produced experimentally), and using like statistical figure of merit the sensitivity obtained (limit of detection), weighted by the delivered surface doses. Typically, for in vivo analysis of X-ray spectroscopy has pre-defined the maximum surface doses at values lower than 10 mGy (Wielopolski, 1999). However, a study to minimize radiation exposure necessary for obtaining a given sensitivity, according to the ALARA principle (As Low As Reasonably Achievable) (U.S. NRC, 2015) becomes mandatory to implement this technique as a future routine clinical analysis. As far as the authors know, this is the first report of experimental configurations achieving successful measurements in the range of the future clinical expected concentration (0.010 mg/ml) (Hainfeld et al., 2011; Khlebtsov and Dykman, 2011) with a measured dose lower than 10 mGy.

2. Methodology

2.1. Bench-top L-XRF system

The setup used for GNPs detection was developed and characterized by FXR laboratory at Universidad de La Frontera (Díaz et al., 2015; Figueroa et al., 2014; Santibañez et al., 2016b) (see Fig. 1a). The essential parts are: 1) Amptek mini-X-ray tube model Mini-X with a tube voltage of 10–40 kV and tube current of 5–200 μA. The tube is equipped with a transmission target made of silver with a thickness of 0.75 μm and a beryllium output window of 127 μm. 2) Amptek Silicon Drift Detector (SDD) model XR-100 SDD connected to Amptek Digital signal processing model PX4. The active zone of the detector has an area of 25 mm^2 and 500 μm of thickness, with an input window made of beryllium measuring 12.5 μm. The resolution of the detector ranges from 125 to 140 eV at 11.2 μs of peaking time for an incident energy value of 5.9 keV. 3) Robotic platform-arm and software for controlling the

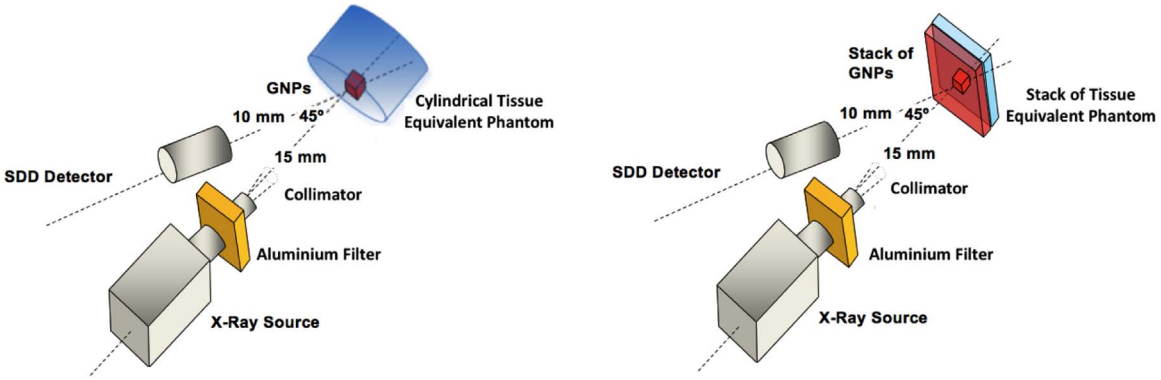

Fig. 1. Geometry of the a) experimental setup, b) simulated setup.

mechanical system for generating 2D images.

The geometry of the setup used considers a source-surface sample distance of 1.5 cm and a sample-detector distance of 1 cm and the source-sample-detector angle was 45° (fixed parameters in the 2D scanning system used). The selected configuration using relative short distances source-sample and sample-detector distance was useful to minimize incident fluence reduction and signal degradation due to air attenuation. Although further clinical implementation may consider different source-sample and sample-detector distances, it was necessary to configure these preliminary experiments according to the available X-ray fluorescence scanning system that works within this distance range. The X-ray tube is equipped with a 2 mm cylindrical collimator in order to reduce beam divergence producing a collimated beam. The beam diameter was 5 mm at the location of the phantom, as measured using radiochromic film. The sample volume considering the collimation of the beam and the detection volume was estimated as 1.4×10^{-1} cm^3.

2.2. Sample preparation

A tissue-equivalent phantom was elaborated with 97% Merck certified cellulose $(C_6H_{10}O_5)_n$ and 3% of Merck certified sodium chloride (NaCl). The 35 mm diameter and 30 mm height cylindrical-shaped phantom provides cavities to place phantom tumor doped with different concentrations of GNPs in tissue equivalent, with a fixed volume of 0.3 cm^3 (See Fig. 2). Additionally, 2 mm thick and 35 mm diameter disks made were constructed with the same material to be located on the phantom surface enclosing the GNPs with the aim of emulating different depths of equivalent soft tissue. The composition of the doped tumor phantoms consisted of mixture of GNPs (15 nm AurovistTM, Nanoprobes Inc.) suspended in deionized water. For the optimization process, a suspension with GNPs concentration of 10 mg/ml was prepared to obtain an intense fluorescent signal. Furthermore, different concentrations within a range of 0.010 mg/ml to 5.0 mg/ml were prepared to obtain the corresponding calibration curve also determining the detection limit of the system.

2.3. Monte Carlo simulation

Monte Carlo simulations were performed with the objective of determining the set of spectra with central energy greater than the edge of absorption L_{III} Au (11.2 keV) that will be implemented experimentally. Spectra obtained by different combinations of kVp and filters were studied by Monte Carlo simulations evaluating whenever the corresponding fluences may by suitable for in vivo applications. Monte Carlo simulations were performed with the open source software XMI-MSIM version 5.0 (Schoonjans et al., 2013, 2012; Vincze et al., 1999). This code is specifically optimized to predict the XRF spectral response in EDXRF systems. Some of the advantages offered, when compared with other similar codes, are the simulation of the M-lines and cascade effects, fluorescence and Compton escape peaks and pulse pile-up (Schoonjans et al., 2012). Additionally, the software is optimized for operating in variance reduction techniques, facilitating its implementation without high computational requirements.

The X-ray source was defined as a series of discrete lines or continuous energy intervals, each with their own energy and intensity with the maximum value in correspondence to the maximum experimental kVp setting. The detection system implemented was a SDD detector of 25 mm^2 in area and 500 μm thick. The electronics parameters, such as gain, zero, Fano factor and electronic noise were set to produce a similar detector response to 9.63 keV in accordance with the real detector used in the experimental setup (FWHM of 251 eV). The number of spectral channels was set to 1024 with a detector gain of 0.0195 keV/channel and a detector zero of 0.0301 keV. The detector response function is included in the database of the software and has been described in previous work by the developers (Vincze et al., 1993, 1999).

The simulated setup is geometrically identical to that experimentally implemented. The simulation considers a source-sample-detector angle of 45°, a source-sample distance of 1.5 cm and a sample-detector distance of 1.0 cm (see Fig. 1b). Several X-ray sources with tube voltages among 10–25 kVp and aluminum filters of different thicknesses (0.50–3.5 mm) for each kVp, were configured to simulate a non-symmetrical narrow spectra with a fixed FWHM (5 keV). Given that the XMI-MSIM code models the samples as stack layers, the simulated tumor doped with GNPs is placed like one of the stacks of the complete (15 mm thick) phantom, formed by a suspension of water and GNPs with different concentrations. The size of the X-ray spot on the surface is fixed by a virtual slit of dimensions similar to the produced by the real X-ray source (20 mm^2). This produces an illuminated volume of 0.3 cm^3 (equal to the tumor phantom designed for the experimental implementation). A second stack formed by a volume of soft tissue of a density of 1.0 g/cm^3, with a thickness of 15 mm, represent the complete phantom studied.

Finally, it is worth mentioning that one of the most relevant information provided by Monte Carlo simulations regards the selection of proper setups for the experimental conditions aimed at LoD optimization.

2.4. Experimental spectrum optimization

Identification and quantification processes in this study were made considering the characteristic fluorescent emission of Gold Lα and Lβ (9.78 keV and 11.5 keV). For the optimization process, dedicated measurements were carried out to determine the optimal incident spectrum that minimized the limit of detection (LoD) and the doses. Different tube voltages (14–23 kVp) and aluminum filter thicknesses (0.75–3 mm) obtained by Monte Carlo simulations, were experimentally configured (see Table 1) to obtain non-symmetrical narrow spectra

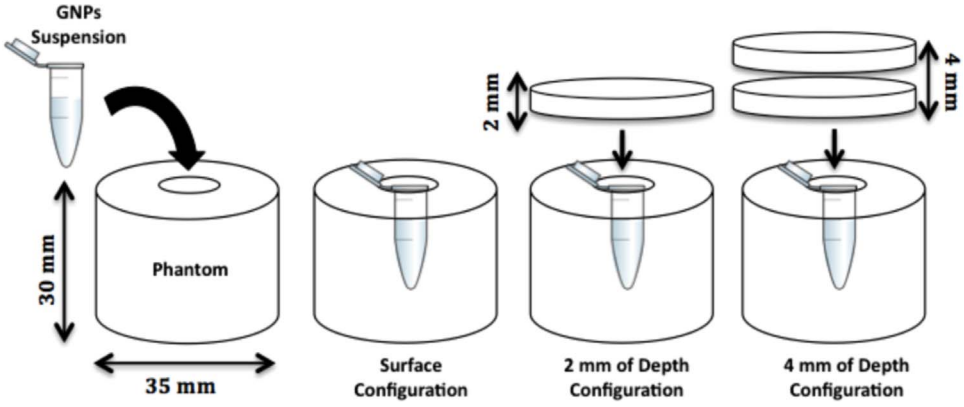

Fig. 2. Configuration of the different tumor and tissue-equivalent phantoms studied at different depths.

Table 1
Parameter of the different X-ray filters and voltage tubes settings for producing different values of central energy at the incident spectrum.

Configuration for different Peak central Energy		
Peak central Energy (keV)	Tube voltage (kV)	Al Filter (mm)
11.2 ± 0.1	14.9 ± 0.1	0.25
13.2 ± 0.1	16.7 ± 0.1	0.50
14.6 ± 0.1	17.9 ± 0.1	0.75
15.6 ± 0.1	18.8 ± 0.1	1.00
16.5 ± 0.1	19.6 ± 0.1	1.25
17.2 ± 0.1	20.3 ± 0.1	1.50
17.9 ± 0.1	20.9 ± 0.1	1.75
18.5 ± 0.1	21.5 ± 0.1	2.00
18.9 ± 0.1	21.9 ± 0.1	2.25
19.4 ± 0.1	22.3 ± 0.1	2.50
20.3 ± 0.1	23.2 ± 0.1	3.00

with fixed FWHM (5 keV) and a central energy ranging from slightly above the gold L-edge (11.2 keV) to a maximum of 20 keV (see Fig. 3). Measurement time was set to 60 s in all cases involving the designed tissue equivalent phantom with a surface cavity of 0.3 cm^3 (Fig. 2), filled with a GNPs suspension of 10 mg Au/ml (Table 2).

The spectral data were analyzed using commercially available software separating the Gold X-ray fluorescent signal and the background from the measured spectrum. The background outside the peaks region was fitted by fourth-order polynomial least-squares fit and further interpolated to obtain the background counts under the X-ray fluorescent peak. These background values were subtracted from each spectrum. A superposition of two Gaussian distributions was fit to each L-XRF peak, corresponding to the $L\alpha_1$-$L\alpha_2$ and $L\beta_1$-$L\beta_2$. The peak position was fixed at the theoretical energy of each fluorescent sub-lines: $L\alpha_1$ (9.71 keV), $L\alpha_2$ (9.63 keV), $L\beta_1$ (11.44 keV) y $L\beta_2$ (11.58 keV). The relative intensities of the peak were fitted using the relative contribution of the gold L-emission: $L\alpha_1$ (100%), $L\alpha_2$ (11%), $L\beta_1$ (68%) y $L\beta_2$ (22%).

The statistical figures of merit used for evaluating the optimal spectrum in order to increase the sensitivity and reduce the radiation dose were determined by the evaluation of the LoD and the dose measurements required for achieving these LoD values. The LoD is a statistical criterion to diminish the detection of a signal in terms of to the background of a certain measurement. In X-ray spectroscopy, it is utilized to determine the presence of elemental chemical substances, in which the peak or signal is statistically discriminable from its

Table 2
Values obtained for the central energy of the optimal incident spectrum for the different depths.

Depth	Lower-LoD	Lower-Dose
0 mm	15.6 keV	17.9 keV
2 mm	16.5 keV	19.4 keV
4 mm	17.2 keV	17.2 keV

background. One of the most applied definitions is given by (Van Grieken and Markowicz, 2002):

$$LoD = \frac{3\sqrt{I_B}}{I_F} C_{Au} \quad (1)$$

Were I_B is the background counts, I_F is the fluorescent signal counts of gold and C_{Au} is the concentration of gold in the sample. *LoD* assessment was performed by Eq. (1).

Calibrated RadCal (Accu-Pro 10x6–6M) ionization chamber was used to measure absorbed dose at phantom surface according to each incident spectrum. The measured absorbed doses along with required irradiation times were further used as input for the *LoD* optimization process.

2.5. Experimental measurement of the detection limit

Although the limit of detection is a statistical criterion that allows evaluating the sensitivity of a system when the measurement is performed in a set of specific parameters, it does not imply that the obtained value can be really measured by the system. In order to determine the minimum concentration that the system can detect in a specific application, it is necessary to determine the detection limit from a calibration curve of the fluorescent counts as a function of the concentration, considering the statistical fluctuation when measuring a blank sample (1.96σ for a 95% confidence level, where σ is the standard deviation of the sample without GNPs) (Manohar et al., 2013).

Experimental detection limit was attained by calibration curves that were performed with several GNPs concentration prepared in the range of 0.0–5.0 mg/ml into the surface cavity of 0.3 cm^3 of the tissue equivalent phantoms and below of cylindrical layer of 2 mm and 4 mm over the tissue equivalent phantom (see Fig. 2), thus simulating a range of GNPs concentrations at different depths.

The samples were measured with two spectra obtained in the optimization process specific for each depth (The Lower-LoD and the

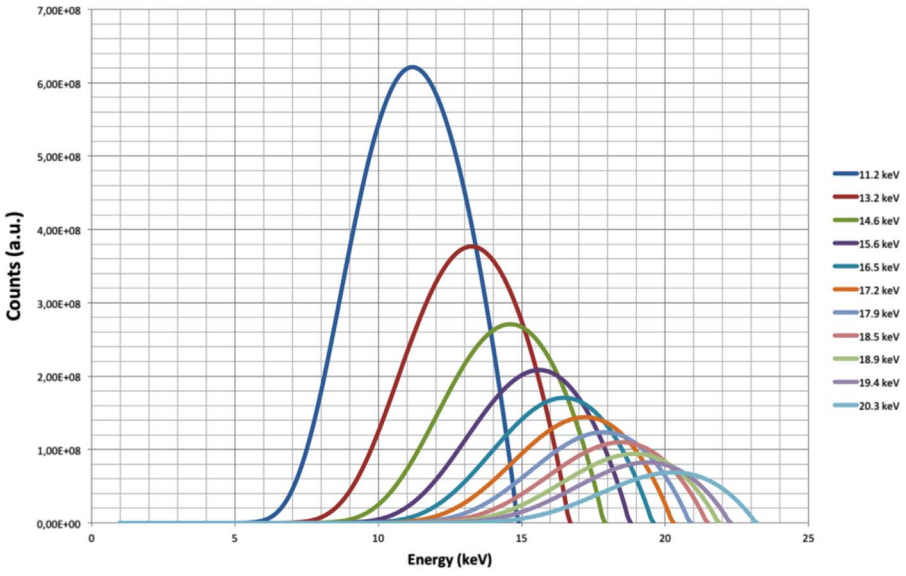

Fig. 3. Incident spectra with different central energy and the same spectral width configured in the Monte Carlo simulation and in the experiments.

Lowe-Dose). Additionally, a sample, which did not include the GNPs, was measured to account for the blank sample and obtaining the calibration curve of the number of fluorescent photons versus the gold concentration. Linear (weighted) least-squares fit was applied to the curve Gold L-XRF signal versus GNPs concentration to obtain the calibration curve. The experimental detection limit was obtained considering the statistical fluctuation of a sample containing no GNPs by using a 95% interval (1.96σ, where σ is the standard deviation of the sample without GNPs). The selected value corresponds to the intersection with the adjustment calibration curve, above which no background signal may affect. Given the low current tube of the X-ray source, for all measurements the surface dose were fixed at 2 mGy, thereby allowing maximum measurement time no longer than 1000 s (estimated time for a routine examination). Future evaluations of systems with power not higher than 20 W (similar kV but a 5 times higher current tube as compared with the system used in the present study) may produce similar sensitivity in shorter measurement times and with surface dose not greater than 10 mGy, which is the typically fixed value for in vivo analysis of X-ray spectroscopy (Wielopolski, 1999).

3. Results and discussions

The scanning energy from 11.2 keV (slightly lower than the L_{III} absorption edge of 11.9 keV) to 20.3 keV shows a qualitative difference between the number of fluorescent counts and the level of background around the peak of interest as function of the central energy of the X-ray spectrum setting and in function of the depths of the tumor phantom (see Fig. 4). This demonstrates the feasibility of finding optimal excitation energy between the two variables. Likewise, MC simulations show similar behavior with the experimental results confirming the potential of models obtained in previous results (Figueroa et al., 2015; Santibañez et al., 2016a).

The behavior of the curves for fluorescent signal versus excitation energy and background signal versus excitation energy was previously explained for similar applications (Figueroa et al., 2015; Santibañez et al., 2016) as follows: As the incident signal obtained in the process is not a pure monochromatic beam, the central energy of the spectrum that maximizes fluorescent production will not be necessarily near the absorption edge. If the central energy of the incident spectrum is shifted from the absorption edge energy to higher values, a higher percentage of photons of the incident spectrum is able to produce fluorescence. However, while all the spectra used have the same spectral width (FWHM), all have different intensities, given the different thicknesses of the filter required to tune each central energy. Therefore, incident spectra with higher central energy have lower fluence than those spectra with less central energy, but having major percentage of photons capable of producing fluorescence. Another issue to be addressed, is that the increment in the central energy of the incident spectrum modifies the percentage of photons having energy high enough to produce photoelectric absorption. The competition among these processes determines the spectrum maximizing fluorescent photon production. On the other hand, the increment in the central energy also causes a shift in the position of the Compton peak (associated to the energy of the incident narrow beam and the geometry detection). Therefore, when the incident spectra increase the central energy a decrease of the background around the region of interest (region of the fluorescent signal) is produced.

The quantitative determination of the fluorescent net counts and background from the recorded spectra, allows to assess a minimum in the *LoD* at different central energies (Fig. 5), for an excitation spectrum with a central energy around 15.6 keV for the tumor phantom in the surface, 16.5 keV at 2 mm of depth and 17.2 keV at 4 mm of depth (white points in the graph). The results are comparisons between the result predicted by the Monte Carlo simulation for the same incident spectrum (black points in the graph) and with the adjusting curve modeled to the simulation. These results exhibit similar behavior for both Monte Carlo and experimental estimations of the energy at which the minimum happens. Experimental uncertainties were assessed according to standard error propagation theory. When the corresponding doses required for achieving the different LoD by the spectrum studied are considering, a new set of optimized spectra is obtained. The best optimizations of the relation LoD/Doses (Lowest-Dose optimization) corresponded to the spectrum with central energy of 17.9 keV in the surface configuration, the spectrum with a central energy of 19.4 keV at 2 mm of depth configuration and the spectrum centering at 17.2 keV for the tumor phantom at 4 mm of depth. Fig. 6 shows the energy shift of the minimum of optimization reached for each of the studied depths. Therefore, two optimized spectrum configurations can be obtained with the application of these criteria: the first, represents the spectrum, which produces directly the Lowest-LoD for a fixed time and the second, represents the spectrum which produces the Lowest-Doses in order to get a similar LoD, but with higher measurement times.

Given the larger attenuation of the fluorescent signal Lα (9.71 keV) in comparison with the Lβ signal (11.4 keV) (see Fig. 7), a rapid decrease of the detection limit is observed increasing the depth of the tumor, as it returns to the Lβ signal at depths above 4 mm (this last measurement is recommended for use in the identification of gold nanoparticles and the Lα only for measurement near the surface). Specifically, when comparing the results obtained in terms of LoD by the two fluorescent signals, which are obtained at the surface and at depths of up to 2 mm, the Lα signal provides a LoD of 33.3–26.7% lower than the Lβ signal. The Lβ signal at 4 mm, however, provides a LoD 10.6% lower and rapidly increases at depths of clinical interest.

The optimization process described above was also performed for the Lβ signal to obtain the respective incident spectra that are optimal for LoD (Lowest-LoD optimization) and optimal in terms of delivered dose (Lowest-Dose optimization). For the surface tumor phantom, the optimum spectrum for LoD was obtained to 17.2 keV and an optimal spectrum for dose at 19.4 keV. Similarly, at depths of 2 mm and 4 mm the Lowest-LoD was obtained to 17.9 and 18.5 keV and the Lowest-Dose

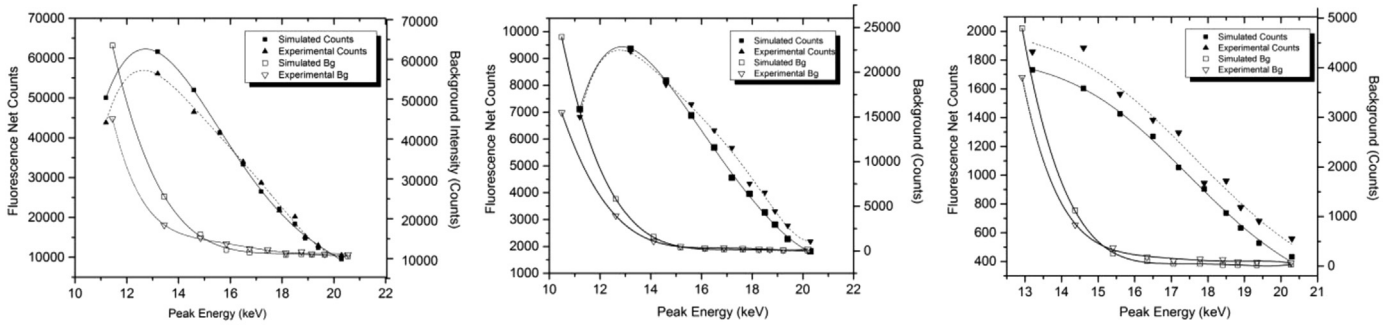

Fig. 4. Detected signal for fluorescent and background photons according to the central energy of the incident spectrum obtained experimentally and by MC simulation for: left) Depth of 0 mm, center) Depth of 2 mm, right) Depth of 4 mm. The dotted and continuous lines represent the fit of the data and show the existence of a maximum for fluorescence and an asymptotic decay for the background.

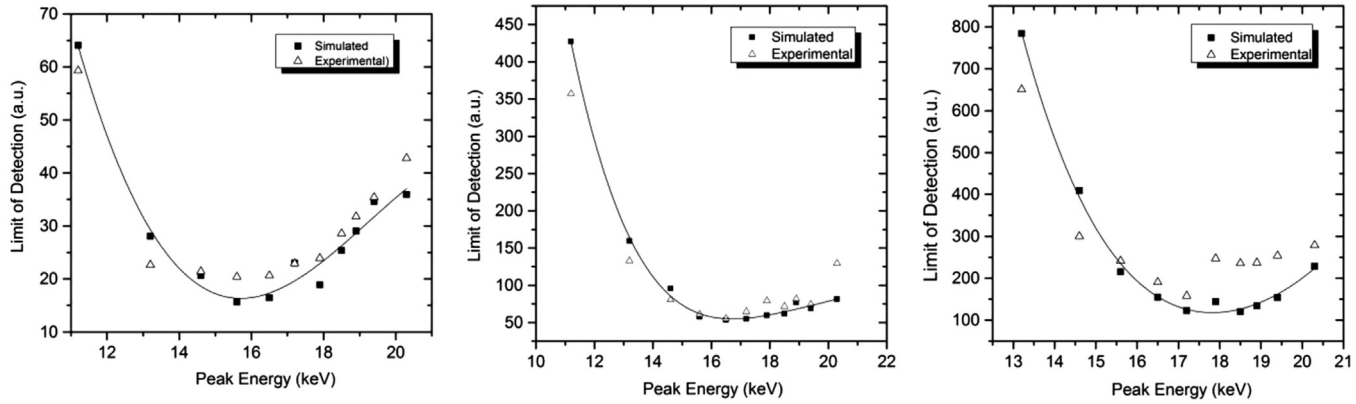

Fig. 5. Experimental measurements (White points) and MC simulations (black points) of the LoD obtained for the Au Lα peak as a function of the central energy of the incident spectrum. The values are for a measurement time of 60 s of phantom tumor of 0.3 cm^3 embedded with 10 mg Au/ml at: left) Depth of 0 mm, center) Depth of 2 mm, right) Depth of 4 mm. Statistical errors are less than 2% and 4% for simulation and experimental data, respectively.

at 19.4 keV for both depths (Figs. 8 and 9 respectively).

Dose rates produced by the optimal spectra at phantom surface obtained for the Lα signal were measured after determining the time necessary to produce a surface dose on the tissue equivalent phantom of 2 mGy. The times obtained for the Lowest-LoD optimization were 444 s, 603 s and 1911 s (to 0, 2 and 4 mm of depth). Similarly, the time necessary to produce the same surface doses by the Lowest-Doses optimization were 987 s, 1911 s (an excessively high time for potential future clinical applications) and 747 s.

The values obtained shows a detection limit for the surface tumor phantom of around 0.010 mg/ml for the setting of Lower-LoD and a detection limit around 0.011 mg/ml for the setting of Lower-Doses (see Fig. 10a and b). These values increase fast at higher depths, showing an experimental detection limit of 0.066 mg/ml and 0.058 mg/ml for the setting of Lowest-LoD and Lowest-Doses respectively at 2 mm of depth (see Fig. 11a and b) and detection limit of 0.118 mg/ml both Lowest-LoD and Lowest-Doses setting at 4 mm of depth (Fig. 12).

The evaluation of the results for the surface measurements show the potential of obtaining high sensitivity, achieving a detection limit in the range of the future clinical expected concentration (0.010 mg/ml) and very close to the most sensitivity system reported in the literature (0.005 mg/ml). Additionally, thanks to the implementation of the X-ray filter and the adjust of the kVp to optimize the sensitivity-dose relationship, the results were obtained with a surface doses lower than the typically pre-defined value used for in vivo analysis of X-ray (2 mGy instead 10 mGy) and allow evaluating a technique according with the ALARA principle. Since this is the first simultaneous optimization of sensitivity and dose for in vivo detection of gold nanoparticles, therefore, don't have reported in the literature about the dose delivered by techniques which reporting similar detection limit values. An approach to evaluate the decrease in the dose provided it is observed considering that the detection limit was achieved by configuring a low power device, one order lower than those used in similar reports (4 W versus typical reports of 50 W of power) in lower measurement times (444 s versus measurements of around 1800 s) and considering the installation of a 1.0 mm aluminum filter.

At first instance, a counter-intuitive result can be observed in the Lowest-Doses optimization for the 4 mm depths. The central energy of the optimum incident spectrum is lower than the obtained for the cases of 0 and 2 mm of depth configurations. Normally, it is expected that at greater depths a beam of higher effective energy will have higher sensitivity given the lower attenuation and therefore a higher number of photons would produce fluorescence (which is true in the range of 0–2 mm depth). However, the generation of this spectrum for larger depths involves filtering the beam to a point that comes into play if the improvement given the greater penetration of the photons of more energy, increase faster than the least quantity of photons with that condition which are produced. This additionally, weighted with the surface dose that generates each one. Therefore, the optimum spectrum would be expected to increase in energy up to a given depth (very superficial 2–3 mm in this case) and from that depth the optimum spectra decay to spectrum with central energy slightly lower for a few more mm of depths, given the poor penetration of the Au L lines which allow analysis only to few mm of depths.

4. Conclusions

According to the obtained results from the optimization process along with experimental measurements, it can be concluded that it is possible to configure a bench-top X-rays system by using an appropriate combination of filters and adjusting the kVp, emitting a narrow spectrum centered on an energy that optimizes the sensitivity and

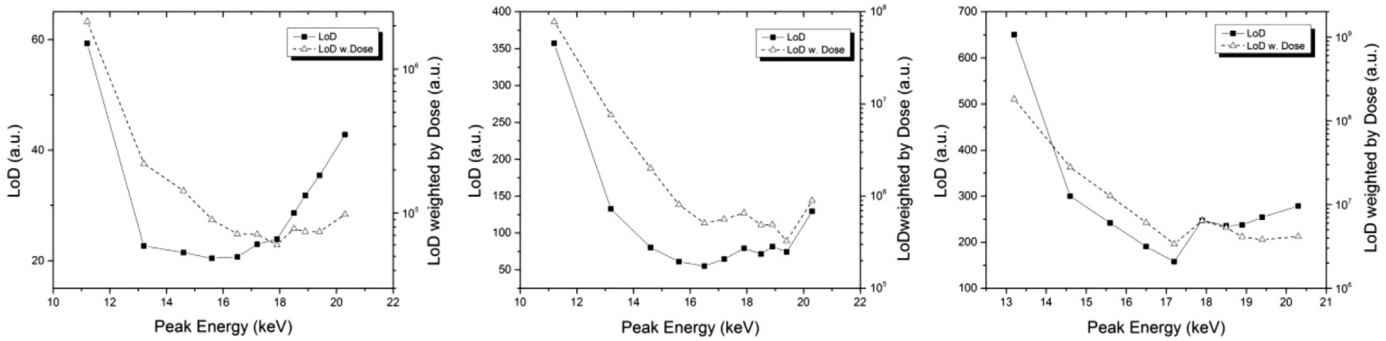

Fig. 6. Comparison between the LoD and the LoD weighted by dose, obtained for the Au Lα peak as a function of the central energy of the incident spectrum. The values are for a measurement time of 60 s of phantom tumor of 0.3 cm^3 embedded with 10 mg Au/ml at: left) Depth of 0 mm, center) Depth of 2 mm, right) Depth of 4 mm.

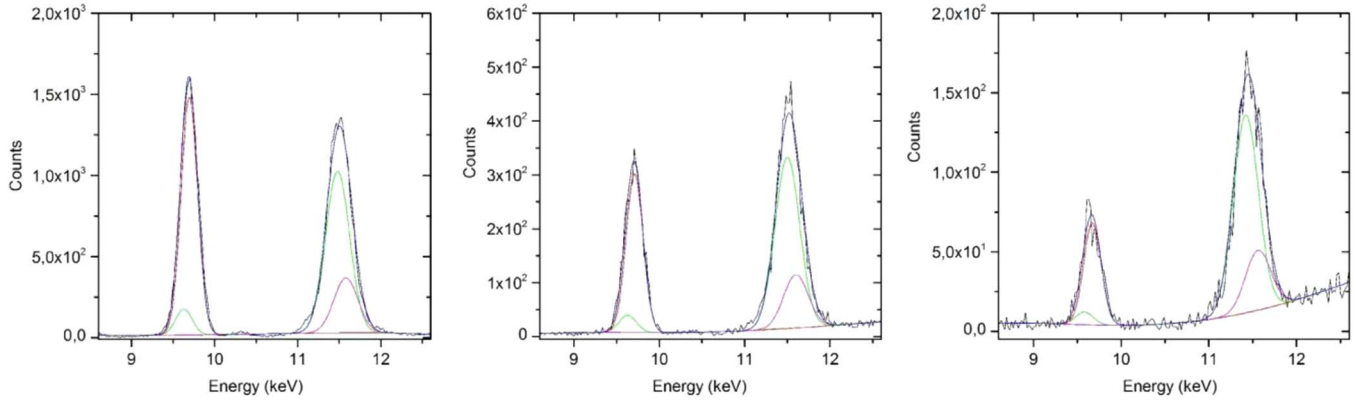

Fig. 7. Measured Lα and Lβ XRF spectra of a 10 mg Au/ml sample acquired at: left) Depth of 0 mm, center) Depth of 2 mm, right) Depth of 4 mm, in tissue equivalent phantom. The blue line represents the fit of the Lα and Lβ signals and the red and green lines represent the fit of the sub-lines Lα1, Lα2, Lβ1 and Lβ2. (For interpretation of the references to color in this figure legend, the reader is referred to the web version of this article.)

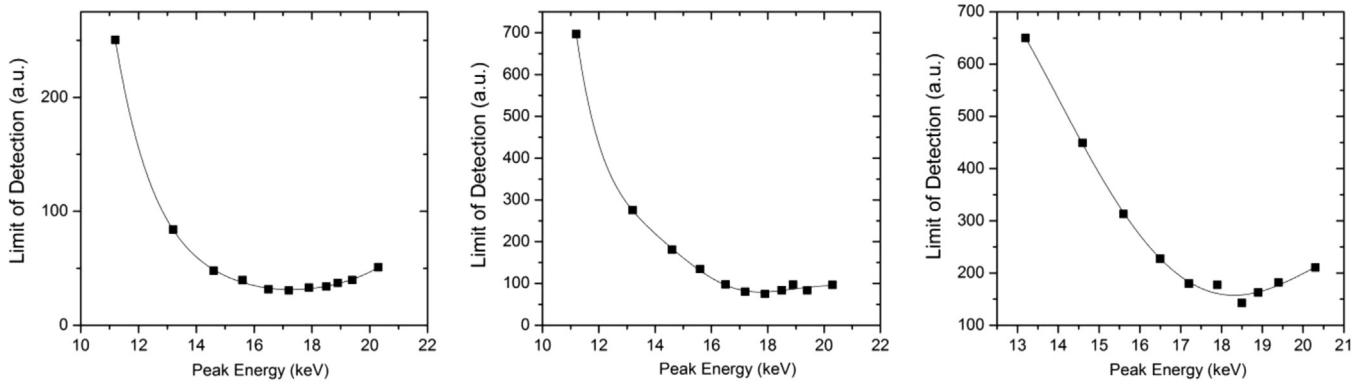

Fig. 8. Experimental LoD obtained for the Au Lβ peak as a function of the central energy of the incident spectrum of a phantom tumor of 0.3 cm^3 embedded with 10 mg Au/ml at: left) Depth of 0 mm, center) Depth of 2 mm, right) Depth of 4 mm, in a tissue equivalent phantom.

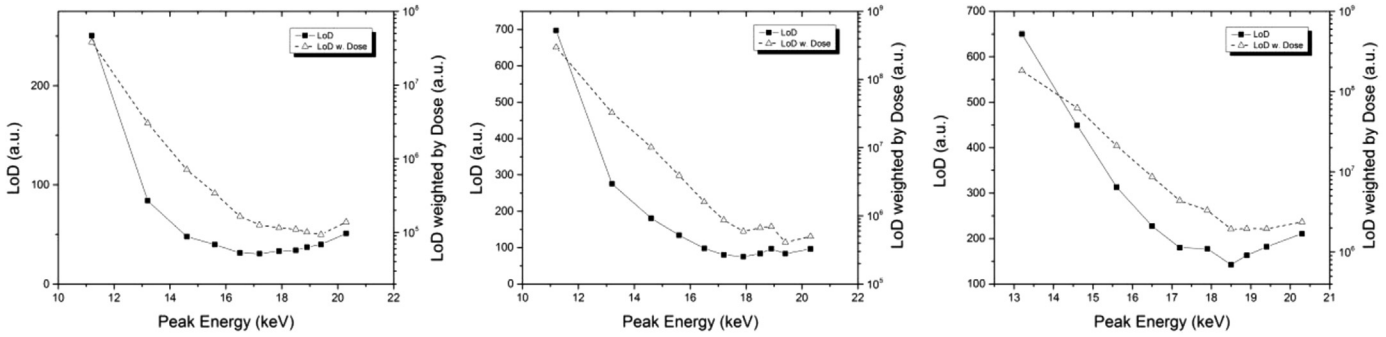

Fig. 9. Comparison between the LoD and the LoD weighted by dose, obtained for the Au Lβ peak as a function of the central energy of the incident spectrum of a phantom tumor of 0.3 cm^3 embedded with 10 mg Au/ml at: left) Depth of 0 mm, center) Depth of 2 mm, right) Depth of 4 mm, in a tissue equivalent phantom.

simultaneously minimizes the entrance (surface) dose delivered during irradiation.

Depending on the required application, the system can be suitably configured to obtain a given detection limit at the lowest dose, for each of the depths studied (17.9 keV at surface, 19.4 keV at 2 mm and 17.2 keV at 4 mm). The optimized spectrum can also be set to the lowest LoD, which will achieve the same desired LoD with a shorter measurement time (15.6 keV at surface, 16.5 keV at 2 mm and 17.2 keV at 4 mm).

The sensibility obtained by the different setting shows a detection limit around 0.010 mg/ml, which correspond to the possible gold concentrations embedded in tumor marker expected to be found in future human in vivo application, and detection limits that increase very fast at larger depths (DL of 0.058 mg/ml to 2 mm of depths and DL 0.117 mg/ml for 4 mm of depths) for fixed doses (2 mGy). Due to the possibility of statistical counts loss and associated increased uncertainty in the settings of very low doses when reaching very low concentration, it is advisable to implement radiation generation systems with a slightly higher power (equal maximum voltage, but 5 times the here implemented tube current) so that, using the same optimization parameters, surface doses would not exceed 10 mGy, as desired (Wielopolski, 1999).

Acknowledgments

This work has been supported by the CONICYT program through FONDECYT grant No. 11150673 and by the Research Division of the Universidad de La Frontera, DIUFRO DI16-2016. The authors R.

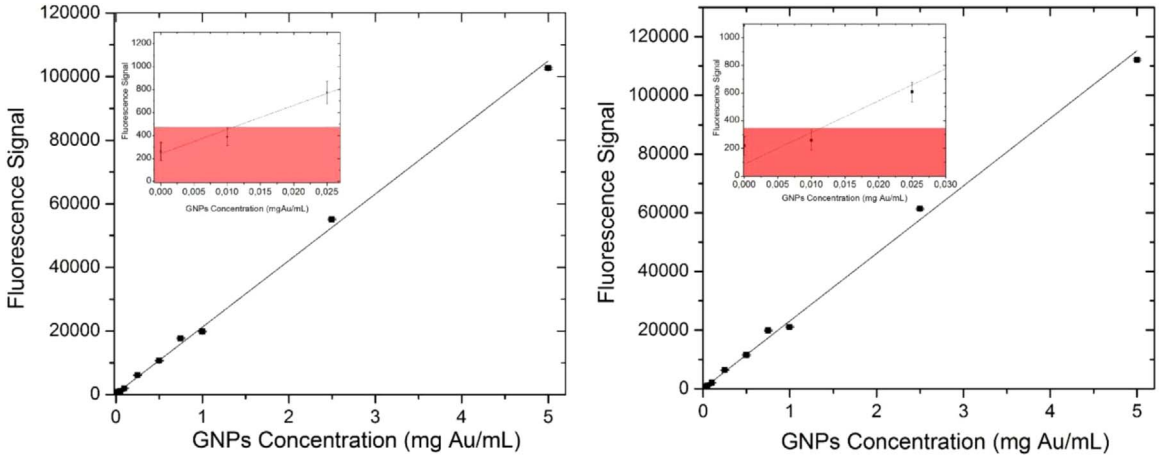

Fig. 10. Calibration curve of Gold L-XRF signal versus the GNPs concentration of tumor phantom at the surface, for the two configurations of the incident spectrum: left) lower LoD, right) lower Dose. The detection limit for the systems is shown in the red zone by the intersection of the weighted linear least-squares fit and the value produced by 1.96σ of the blank sample. (For interpretation of the references to color in this figure legend, the reader is referred to the web version of this article.)

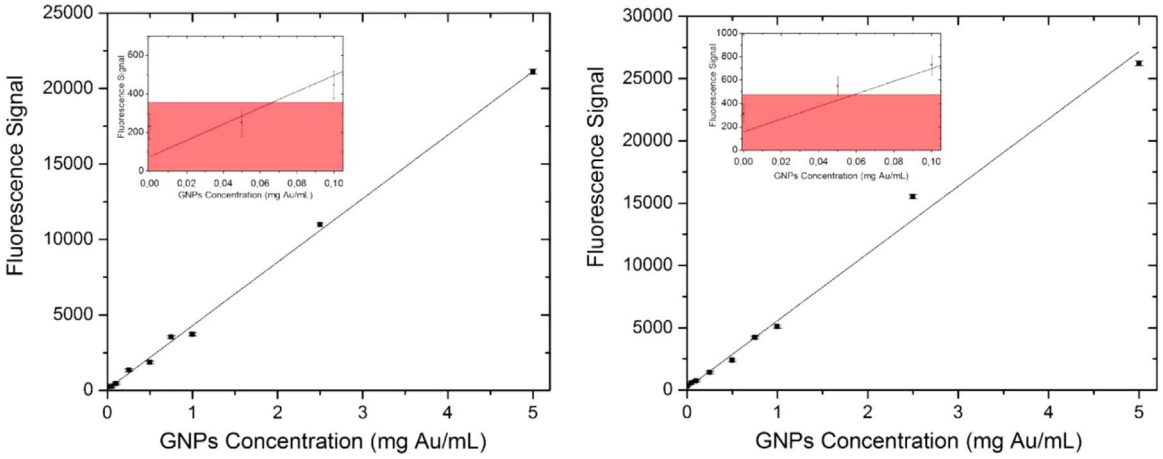

Fig. 11. Calibration curve of Gold L-XRF signal versus the GNPs concentration of tumor phantom at 2 mm of depths, for the two configurations of the incident spectrum (lower LoD and lower Dose). The detection limit for the systems is shown in the red zone by the intersection of the weighted linear least-squares fit and the value produced by 1.96σ of the blank sample. (For interpretation of the references to color in this figure legend, the reader is referred to the web version of this article.)

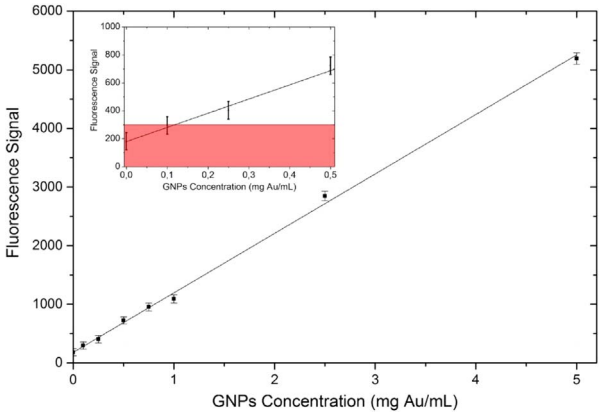

Fig. 12. Calibration curve of Gold L-XRF signal versus the GNPs concentration of tumor phantom at 4 mm of depths, for the two configurations of the incident spectrum (lower LoD and lower Dose). The detection limit for the systems is shown in the red zone by the intersection of the weighted linear least-squares fit and the value produced by 1.96σ of the blank sample. (For interpretation of the references to color in this figure legend, the reader is referred to the web version of this article.)

Saavedra and M. Vasquez would like to thanks CONICYT for scholarships No. 22151920 and No. 22152075.

References

Díaz, A., Parra, C., Valdés, C., Santibañez, M., Figueroa, R.G., 2015. X-Ray Spectrom. 44, 69–674.
Figueroa, R.G., Santibañez, M., Valdez, C.N., Valente, M., 2015. Radiat. Phys. Chem. 117, 198–202.
Figueroa, R.G., Lozano, E., Belmar, F., Alcaman, D., Von Bohlen, A., Oliveira, C.A.B., Silva, A.L.M., Veloso, J.F.C.A., 2014. X-Ray Spectrom. 43, 126–130.
Hainfeld, J.F., Smilowitz, H.M., O'Connor, M.J., Dilmanian, F.A., Slatkin, D.N., 2013. Nanomedicine 8, 1601–1609.
Hainfeld, J.F., O'Connor, M.J., Dilmanian, F.A., Slatkin, D.N., Adams, D.J., Smlowitz, H.M., 2011. Br. J. Radiol. 84, 526–533.
Hainfeld, J.F., Dilmanian, F.A., Zhong, Z., Slatkin, D.N., Kalef-Ezra, J.A., Smilowitz, H.M., 2010. Phys. Med. Biol. 55, 3045–3059.
Hainfeld, J.F., Slatkin, D.N., Focella, T.M., Smilowitz, H.M., 2006. Br. J. Radiol. 79, 248–253.
Hainfeld, J.F., Slatkin, D.N., Smilowitz, H.M., 2004. Phys. Med. Biol. 49, 309–315.
Khlebtsov, N., Dykman, L., 2011. Chem. Soc. Rev. 40, 1647–1671.
Manohar, N., Jones, B.L., Cho, S.H., 2014. Med. Phys. 41, 101906.
Manohar, N., Reynoso, F., Cho, S., 2013. Med. Phys. 40, 080702.
Ngwa, W., Kumar, R., Sridhar, S., Korideck, H., Zygmanski, P., Cormack, R.A., Berbeco, R., Makrigiorgos, M., 2014. Nanomedicine 9, 1063–1082.
Popovtzer, R., Agrawal, A., Kotov, N.A., Popovtzer, A., Balter, J., Carey, T.E., Kopelman, R., 2008. Nano Lett. 8, 4593–4596.
Ren, L., Wu, D., Li, Y., Wang, G., Wu, X., Liu, H., 2014. Med. Phys. 41, 031902.
Ricketts, K., Guazzoni, C., Castoldi, A., Royle, G., 2016. Nucl. Instrum. Methods Phys. Res. A. 816, 25–32.

Ricketts, K., Guazzoni, C., Castoldi, A., Gibson, A.P., Royle, G.J., 2013. Phys. Med. Biol. 58, 7841–7855.
Ricketts, K., Castoldi, A., Guazzoni, C., Ozkan, C., Christodoulou, C., Gibson, A.P., Royle, G.J., 2012. Phys. Med. Biol. 57, 5543–5555.
Santibañez, M., Vásquez, M., Figueroa, R.G., Valente, M., 2016a. Radiat. Phys. Chem. 122, 28–34.
Santibañez, M., Díaz, A., Figuero, R.G., 2016b. X-Ray Spectrom. 45, 92–99.
Schoonjans, T., Vincze, L., Sole, V.A., Sanchez del Rio, M., Appel, K., Ferrero, C., 2013. Spectrochim. Acta Part B 82, 36–41.
Schoonjans, T., Vincze, L., Sole, V.A., Sanchez del Rio, M., Brondeel, P., Silversmit, G., Appel, K., Ferrero, C., 2012. Spectrochim. Acta Part B 70, 10–23.
U.S. NRC. 2015. ALARA principie. Code of Federal Regulations. Title 10, Section 20.1003. (10 CFR 20.1003).
Van Grieken, R., Markowicz, A., 2002. Handbook of X-ray Spectrometry, 2nd ed. Marcel Dekker, New York.
Vincze, L., Janssens, K., Vekemans, B., Adams, F., 1999. Spectrochim. Acta Part B 54, 1711–1722.
Wielopolski, L., 1999. Adv. X-Ray Anal. 41, 892–897.
Wu, D., Li, Y., Wong, M.D., Liu, H., 2013. Med. Phys. 40, 051901.